

Determining the muon mass using a scintillator-based detector

Neal Woo and John Essick

Citation: [American Journal of Physics](#) **85**, 611 (2017); doi: 10.1119/1.4984811

View online: <http://dx.doi.org/10.1119/1.4984811>

View Table of Contents: <http://aapt.scitation.org/toc/ajp/85/8>

Published by the [American Association of Physics Teachers](#)



American Association of **Physics Teachers**

Explore the **AAPT Career Center** – access hundreds of physics education and other STEM teaching jobs at two-year and four-year colleges and universities.

<http://jobs.aapt.org>



Determining the muon mass using a scintillator-based detector

Neal Woo and John Essick^{a)}

Physics Department, Reed College, Portland, Oregon 97202

(Received 9 November 2016; accepted 18 May 2017)

A scintillator-based detection system, of the type employed in the popular muon-lifetime instructional lab experiment, is used to measure the muon mass. The photomultiplier pulse pairs produced by the decay of cosmic ray muons into product electrons and positrons within the scintillator are detected by a digitizing oscilloscope and the energies of the product particles are quantified by integrating the area under their associated pulses. The observed distribution of product-particle energies is then compared with Monte Carlo simulated distributions assuming different values of the muon mass $m_\mu c^2$, where the modeling of product-particle energy loss within the scintillator accounts for collisional and radiative effects in a detailed way. Via a least-squares comparison, it is found that the simulated distribution based on a value of $m_\mu c^2 = 105 \pm 5$ MeV most closely matches the experimental distribution. © 2017 American Association of Physics Teachers. [<http://dx.doi.org/10.1119/1.4984811>]

I. INTRODUCTION

In the advanced instructional laboratory of many physics departments, students use a scintillator-based detection system to measure the mean muon lifetime τ_μ .^{1–7} In this popular experiment, a *start pulse* produced by a cosmic-ray muon being stopped in the scintillator switches on a timer. The timer then marks time until it receives a *stop pulse*, which is due to the fast-moving charged product particle (an electron or a positron, depending on whether the initial particle is μ^- or μ^+) produced in the decay event. The time span between the start and stop pulses gives the decay time t for a given decay event and it is well known that the probability density $P(t)$ of decay times for a large number of events is given by

$$P(t) = \frac{1}{\tau_\mu} e^{-t/\tau_\mu}. \quad (1)$$

This equation implies that 95% of decay times fall within the range $0 \leq t \leq 3\tau_\mu$. Statistical analysis of decay-time data taken using the scintillator-based detection system then yields an accurate value for τ_μ . For the lifetime experiment, the detailed shape of the start and stop pulse is ignored; only the leading edge of the start and stop pulse is used to initiate and terminate the timing process, respectively.

In previous work,⁸ we described a spark chamber setup that can be used to measure the muon mass $m_\mu c^2$. In that experiment, a muon-decay event is recorded photographically as a kinked spark trail produced by the muon and its product particle. The image of this trail is then analyzed (by counting the number of sparks produced) to yield a value for the product's initial energy E_e . Through data acquired on a sizable number of decay events, the experimental distribution of E_e -values can be compared to the predicted distribution from Fermi's description of muon decay, resulting in a value for $m_\mu c^2$.

To account for two facts—some product particles escape the spark chamber before being completely stopped and product particles travel through the spark-chamber plates over a (fairly small) range of angles—a Monte Carlo data analysis method was developed to process the spark-chamber data. We found that, by limiting our data set to include only events that began within an inner portion of the

chamber (termed the *fiducial volume*), the effect of escaping product particles could be minimized, reducing the level of accuracy required for our simulation. Then, basing our Monte Carlo simulation on a simple model that assumed charged product particles travel in straight lines as their lost energy is completely absorbed by the chamber's aluminum plates, we obtained an accurate result for $m_\mu c^2$.

In this paper, we show how a scintillator-based detection system of the type employed in the popular muon-lifetime experiment can be used to carry out the more difficult task of measuring the muon mass. To accomplish this task, the shape of the pulse produced by a product particle is used to determine its initial energy E_e . As in the spark-chamber experiment, the experimental distribution of E_e -values acquired for a large number of decay events is then compared to the predicted distribution of a Monte Carlo simulation, resulting in a value for $m_\mu c^2$.

In Secs. II–VI, we first review Fermi's theory of muon decay, and then describe our experimental scheme for observing muon decay events. Next, we summarize the theory of energy loss experienced by charged particles traversing matter, and then we outline the basis of our Monte Carlo simulation. Finally, we analyze our data to determine the muon mass $m_\mu c^2$ (as well as the mean muon lifetime τ_μ).

II. FERMI THEORY OF MUON DECAY

Almost all muons μ^- and antimuons μ^+ decay via the following two modes:

$$\mu^- \rightarrow e^- + \nu_\mu + \bar{\nu}_e \quad (2)$$

and

$$\mu^+ \rightarrow e^+ + \nu_e + \bar{\nu}_\mu, \quad (3)$$

where we will generically call the electron and positron the *product particle* (or *product*, for short) of muon and antimuon decay, respectively. Also, henceforth, we will use the term *muon* to describe both μ^- and μ^+ particles.

Because muon decay produces two neutrinos in addition to the product, the product is created with an initial energy E_e not uniquely determined by conservation laws. Instead, this energy falls into a range of allowed E_e -values. The

minimum value of this range is $E_e = 0$ (neglecting the particle masses), in which case the product is at rest and the two neutrinos move oppositely directed with equal momentum magnitude. At the other extreme, the maximum product energy occurs when both neutrinos move in the opposite direction to the product. Then, assuming the muon is much more massive than all of the other particles, it is easy to show from the conservation laws that $E_e = \frac{1}{2}m_\mu c^2$. Thus, the allowed range of product energies is $0 \leq E_e \leq \frac{1}{2}m_\mu c^2$. The Fermi description of muon decay via the weak interaction,⁹ in which the decay (in lowest order) is mediated by a W boson, yields the following relation for the probability density $P(E_e)$ of the product being produced with energy E_e :

$$P(E_e) = C(m_\mu c^2 E_e)^2 (3 - 4E_e/m_\mu c^2), \quad (4)$$

where C is a constant. Higher order radiative effects (due to the exchange of a virtual photon by the muon and product particle) modify this expression slightly¹⁰ as shown in Fig. 1. Note from this plot that product particles of muon decay are more often created with initial energies near the higher end of the range of allowed E_e -values.

III. DESCRIPTION OF EXPERIMENT

A. Scintillator-based detection system

Our detector consists of a cylindrical EJ-200 plastic scintillator with 10-cm radius and 40-cm height, coupled to an ETEL 9390KB photomultiplier tube (PMT) via a 4-inch thick PMMA light guide.¹¹ The scintillator and light guide are both wrapped in a light-tight black vinyl cover with an internal reflective layer to enhance light collection efficiency. The material EJ-200 is a polyvinyl-toluene (PVT) based scintillator that is doped with anthracene as the primary fluorescent component. Like most plastics, EJ-200 has very fast timing, with a decay time of 2.1 ns. Its emission spectrum is well-matched to the PMT's quantum efficiency profile. The PMT has 10 dynodes, providing a gain of $g = 7 \times 10^5$ when biased at 1000 V. It has two signal outputs available: the anode and the last dynode. We use the signal from the last dynode, which is better for energy information.

For a muon decay occurring in the scintillator volume, the product particle is emitted in a random direction and with initial energy E_e . As this charged product traverses the detector, it deposits energy through collisional and radiative

electromagnetic interactions with the constituent atoms, which the scintillator reradiates as light. This light is funneled to the PMT where it is converted to an output electrical pulse, the area under which we take to be proportional to E_e . For this method to be valid, it is critical that the detector produces the same shape pulse for a product particle with given E_e , regardless of the proximity of the particle's path to the PMT. To ensure a flat response with regard to location of the events within it, the detector's design included light-collection compensation. By placing a circular blocking mask of reflective film at the center of the PMT entrance window and adjusting the reflective properties of the scintillator's surfaces, light from events at all locations within the detector is forced to travel approximately the same path length into the PMT. Tests using equal-energy electrons created by a collimated beam of Cs-137 gamma rays incident at differing positions within the detector produced almost identical pulse amplitude and shape, confirming successful light collection compensation.

The dynode output signal of the PMT was monitored on a single channel (with 50- Ω input termination) of a low-cost Tektronix TDS 2024 digital oscilloscope, which has a maximum sampling rate of 2 GS/s. This allows us to resolve the sub-microsecond PMT pulses into enough data points for accurate analysis. A LabVIEW data-taking program was developed to communicate with the oscilloscope and search for decay events in the PMT signal.¹² The experimental setup is illustrated as a block diagram in Fig. 2.

B. Outline of experimental procedure

Our experimental scheme to measure $m_\mu c^2$ is as follows. By benefit of the time dilation effect, high-speed muons created in the upper atmosphere travel to Earth's surface, where they are incident on our detector. Though the majority of these muons have such high energy that they are simply slowed as they pass through and then exit the detector, those muons with sufficiently low energy (≤ 90 MeV) are stopped in the scintillator. In either case, the incident charged muon will lose energy to the scintillator, resulting in a PMT pulse. However, those muons that are stopped will decay on average 2.2 μ s later, each producing a product particle (an electron e^- or positron e^+) and two neutrinos (that pass out of the scintillator undetected). As described in Sec. III A, the product then moves and is slowed in the scintillator, producing a PMT pulse. Thus, the signature of a muon decay event is two PMT pulses within several μ s of each other as shown in Fig. 2.

Our innovation is to measure the initial energy E_e of the product particle by analyzing the shape of the second pulse. Assuming that the scintillator's light output response is linearly related to the deposited energy of the e^\pm , and that the PMT amplifies pulses in a linear manner, we can obtain a relative measurement of E_e from the integrated area under the PMT's associated output pulse. Ideally then, the experimentally observed distribution of E_e -values is determined by observing a large number of decays, and a fit of this experimental data to the theoretical relation for $P(E_e)$, given in Eq. (4), allows extraction of $m_\mu c^2$ as a fit parameter.

Unfortunately, as was the case in our spark chamber experiment, the finite size of our detector prevents a straightforward application of the above-described scheme. Depending on where a decay event occurs within the scintillator and in which direction the resulting product particle travels, the

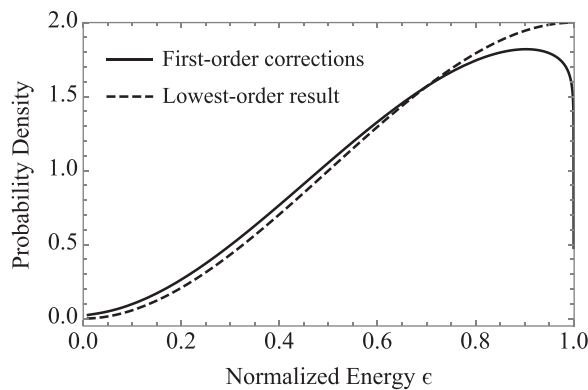


Fig. 1. Fermi theory prediction for energy spectrum of product particles produced in muon decay, in lowest-order (dotted) and with first-order radiative effects (solid) over normalized energy $\epsilon = E_e/E_{\max}$, with $E_{\max} = \frac{1}{2}m_\mu c^2$.

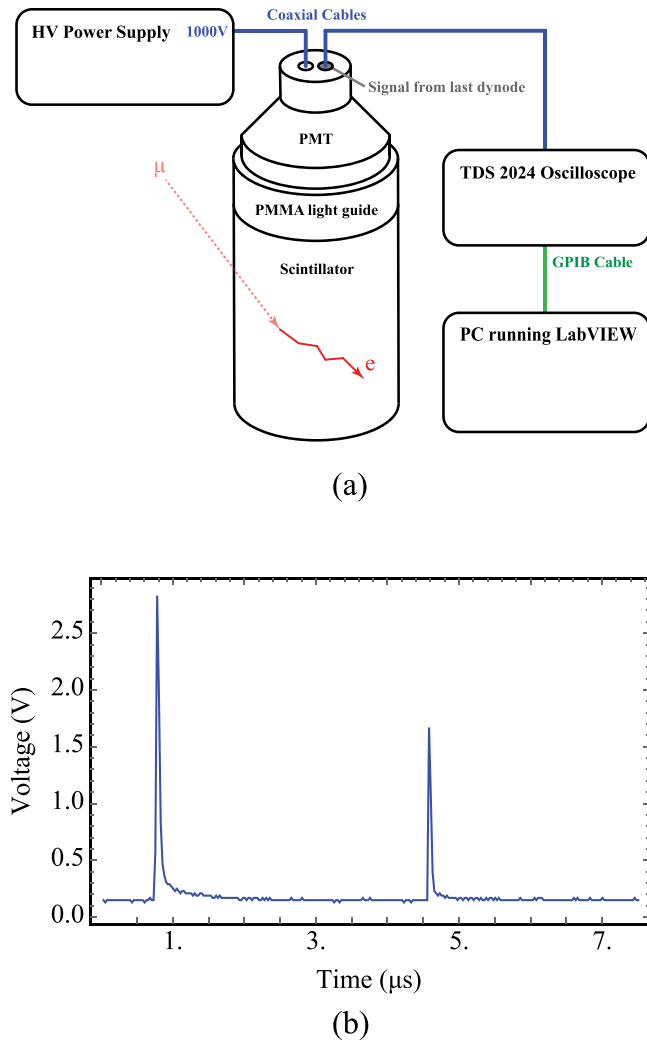


Fig. 2. (a) Diagram of the experimental setup, which includes a scintillation detector, digitizing oscilloscope for signal readout, and LabVIEW software for signal processing and data storage. (b) The PMT's dynode output signal for a muon decay event. The first pulse is produced as the muon is brought to rest in the scintillator, depositing its kinetic energy. Within a few microseconds, the muon decays to produce a charged product particle, which deposits its kinetic energy and generates a second pulse.

product may escape the scintillator volume before being stopped. Such escaping particles deposit only a fraction of their initial energy in the scintillator and so produce PMT pulses that are characteristic of lower energies than the product's true E_e -value. This *product-escape* effect distorts the observed energy distribution from the ideal form of Eq. (4). We note that Eq. (4) predicts that higher-energy e^\pm are more often produced and it is these higher-energy particles that travel farthest in the detector and have the greatest chance to escape with some remaining energy. Thus, the product-escape effect disproportionately causes higher-energy events to appear in the lower-energy end of the observed spectrum, obscuring the underlying theoretical distribution.

Product escape is a geometric effect that is manifested statistically over a large number of events and it is not tractable to account for this effect analytically. However, such problems lend themselves well to Monte Carlo methods.¹³ Thus, to account for product escape theoretically, we randomly create in software a large number of decay events scattered through the scintillator volume and calculate the energy

deposited in the detector for each assumed event using a model of product transport, yielding a prediction for the observed distribution of product energies. For each simulated distribution, we assume a value for $m_\mu c^2$ from which the initial product energies are sampled consistent with Eq. (4). Whichever $m_\mu c^2$ -simulated distribution most closely matches the observed data then yields the true value of $m_\mu c^2$.

Interestingly, the product-escape effect is expected to aid in this process of determining the muon mass. As noted previously, the distribution of E_e -values is skewed toward the maximum value of $E_{\max} = \frac{1}{2}m_\mu c^2$, and it is these faster moving product particles that are most likely to escape the detector before being stopped. Since the choice of $m_\mu c^2$ determines the value of E_{\max} , we anticipate that as $m_\mu c^2$ is chosen to be larger and larger, the higher-energy portions of the resulting simulated distributions will be more and more suppressed. In short, since $m_\mu c^2$ is implicitly tied to differing levels of the product-escape effect, as we vary the assumed muon mass value, the qualitative shape of simulated distributions will differ in a marked way, easing our decision of the best-fit simulation to our observed data.

C. Data acquisition

PMT pulses were recorded by our computer-controlled digital oscilloscope, which has a fixed record length of 2500 points. The scope was configured in its single-acquisition mode and set to trigger on a large-amplitude muon-generated pulse. Then, by appropriate choice of scope settings, the product-produced pulse was acquired in the recorded time window after the trigger. Each scintillator pulse has a dominant ns-timescale component, followed by a small-amplitude μ s-timescale tail. We found that to fully resolve muon and product pulses, they must be separated by $\geq 0.5 \mu$ s. We selected the scope's trigger position so that the leading edge of muon pulse was 0.5μ s prior to the recorded window, i.e., only the product's pulse was recorded on the scope trace. The scope's 500 ns/DIV timebase setting then allowed us to capture a 2500-point waveform over a time window ranging between 0.5 and 5.5μ s after the muon pulse, enabling us to capture the majority ($\sim 75\%$) of decay events.

To minimize the programming overhead of transferring every acquired trace over the GPIB interface into computer memory, we used the scope's internal waveform-maximum measurement function to determine if a product-produced pulse was present in the current trace. If the waveform's maximum value exceeded $3 \times$ the noise level (including any residual of the muon pulse), we assumed a product pulse was present and the trace was transferred and stored in a computer file; if the maximum value was below this chosen $3 \times$ threshold, we assumed the trace was simply noise (i.e., the triggering muon passed through the detector without decaying) and the trace was not transferred. By this method, we were able to acquire and evaluate about two traces per second, with about one of these traces having a product pulse every two minutes. Typical data runs lasted 120 h and yielded 3500 stored product-pulse waveforms, which were analyzed after the conclusion of the run.

IV. MONTE CARLO SIMULATION

Initially, our intent was to analyze the data collected from our scintillator-based detector using the simple Monte Carlo modeling previously developed for our spark-chamber

experiment. However, we discovered that this simplified model consistently predicted a greater number of high-energy product pulses than was observed in our present experiment. We soon realized that there were a number of favorable features in the spark-chamber setup that allowed the simple model to account for the product-escape effect accurately enough to produce good results, but that these features were not inherent to our scintillator-based system. Namely, the images of muon decay produced in the spark-chamber experiment allowed us to restrict our final data set to events that occurred within the interior region (“fiducial volume”) of the chamber, suppressing the product-escape effect in our data. The output of the scintillator experiment is simply electrical pulses with no knowledge of where these signals originate within our detector and so there is no provision for defining a fiducial volume. In addition, the spark-chamber tracks are confined to be within about 30° from the chamber’s vertical axis, giving a natural restriction of product-escape images in our data set. In contrast, the scintillation detector will produce pulses for charge movement at all angles, greatly enhancing the chance of signals in our data set produced by product-escape events. Finally, the absorbing power of aluminum used for the spark-chamber plates is greater than the lower-density plastic scintillator used for this present experiment. Hence, stopping distances are greater for both charged particles as well as the radiation they produce, leading to more likely energy escape from the plastic detector, especially for higher-energy events. For these reasons, we were led to conclude that a detailed accounting of energy-loss mechanisms is needed to properly model the data acquired from our plastic scintillator-based detector.

Using Mathematica, we wrote a Monte Carlo program to model product-particle transport in our polyvinyl-toluene plastic scintillator. In writing this code, we incorporated approaches used in GEANT4,¹⁴ the program commonly used to simulate the passage of particles through high-energy physics detectors, as well as EGSnrc¹⁵ and PENELOPE,¹⁶ programs that model radiation transport in medical applications. Our code is valid for product energies up to ~ 200 MeV, well within the upper bound set by $E_{\max} = \frac{1}{2}m_\mu c^2$ for all of our choices of $m_\mu c^2$. Tables of integrated cross sections are used by the code to quickly interpolate cross sections and other relevant quantities as the particles are simulated. Here, we provide a brief description of the code; a reference manual with thorough discussion of the technical details is available as a supplement to this paper, as is the Mathematica code.¹⁷

A. Passage of electrons and positrons in matter

As a charged particle passes through matter, it experiences kinetic energy loss and path deflection due to electromagnetic interactions with the constituent nuclei and electrons of the material.^{18,19} For a heavy particle such as a proton or pion, inelastic collisions with atomic electrons result in excitation or ionization of the latter; the requisite energy driving these processes comes at the expense of the incident particle, causing it to slow down. As it travels, the incident particle suffers a high number of low-energy-transfer collisions, and the resulting average energy loss per unit path length is well-described by the Bethe-Bloch Formula. In addition, the particle is deflected by many small-angle scatters from elastic collisions with atomic nuclei; over sufficient distance, the net scattering distribution is Gaussian via the central limit

theorem, with less frequent large-angle scatters contributing non-Gaussian tails. Thus, heavy charged particles traversing matter experience energy-loss and path-deflection by separate processes, whose net effects can be treated with statistical methods.

Lighter particles such as e^\pm undergo a much more tempestuous path as they traverse matter. As with heavy particles, an e^\pm traversing matter loses energy to inelastic collisions with atomic electrons. In addition, energy may be lost to radiative processes in the form of bremsstrahlung photon emission, which becomes the dominant mode of energy loss at increasingly higher particle energies. Due to their light mass, it is not uncommon for an e^\pm to lose a significant fraction of its energy in a single collisional or radiative event, dubbed a “hard” event. The increased presence of hard events causes the average energy loss per unit path length to fluctuate in a way that is more difficult to treat statistically. Likewise, elastic collisions more often result in large-angle deflections, so the net scattering over many events is not necessarily Gaussian.

Due to the extremely high number of interactions experienced by the e^\pm , it is not computationally feasible to simulate every interaction explicitly. At the same time, accuracy may be lost if energy-loss and path-deflection are treated solely in their net effects for the reasons previously mentioned. Following the lead of commonly used simulation programs, we simulate e^\pm transport by a *mixed-class* approach, where hard events with energy loss above a specified threshold are simulated discretely, while the net effects of sub-threshold “soft” events are treated continuously. This achieves a balance between computational efficiency and predictive accuracy.

B. Electron and positron interactions

In our simulation, electrons and positrons are assumed subject to Møller, Bhabha, and bremsstrahlung interactions. Inelastic collisions of these product particles with atomic electrons are treated on the basis of the Møller (e^-e^-) and Bhabha (e^+e^-) scattering cross sections.^{18,20} The cross sections are integrated with respect to the energy-transfer T between incident and target particles in two energy regimes: from zero energy up to some specified cutoff value T_c to determine the average energy loss per unit path length from soft events, then from T_c to the maximum allowed energy transfer T_{\max} to determine the mean free path between hard events. The energy lost to soft collisions is considered to be deposited continuously along the path of the product. Hard inelastic collisions between an incident product and an atomic electron result in the ejection of the electron from its atom with kinetic energy $T > T_c$, if the product is a positron, or $T > 2T_c$, if the product is an electron (in which case incident and target particles are indistinguishable). This high-energy ejected electron is termed a *secondary electron*, and its energy loss along the path it follows through the scintillator must also be calculated.

The same approach is used for bremsstrahlung cross sections, where we define a photon cutoff energy k_c . Hard radiative events result in the creation of a photon with energy $k > k_c$, while soft radiative events are expressed as continuous energy deposition along the path of the product.

The cutoff energies T_c and k_c are selected such that the average range of particles below the cutoffs are small, relative to the dimensions of the detector. We used

$T_c = 0.2 \text{ MeV}$ and $k_c = 0.01 \text{ MeV}$, for which the electron range is $\sim 0.05 \text{ cm}$ and the photon mean free path is $\sim 0.5 \text{ cm}$. Positrons experience the additional interaction of two-photon annihilation, which is simulated explicitly either in-flight or at the end of the positron's trajectory.

The trajectories of electrons and positrons are calculated in iterative *steps* as follows: the particle with kinetic energy E is moved forward by a given step length s , the energy loss from soft collisions over s is subtracted from E , and the modification of the trajectory due to the multiple elastic scattering (see below) is determined. After each step, an event prediction routine determines whether a hard event occurs based on the macroscopic cross sections of the interactions in play. If it is determined that a hard event of a certain type occurs, the product energy and trajectory are modified accordingly.

Step lengths for e^\pm are selected by forcing the combined energy loss due to soft collisional and radiative events not to exceed a given fraction f of the particle's energy at the beginning of the step. For example, if we set $f = 0.05$, then s is chosen to be the distance over which the particle must travel in order to deposit one-twentieth of its energy. This procedure prevents the energy-dependent cross sections from varying too drastically over a single step.

The net angular deflection and lateral displacement of a product particle due to multiple elastic scattering over a step s is treated by the random hinge method developed by Bielajew.¹⁶ In this method, all of the elastic scattering events resulting in angular deflection and lateral displacement of the particle are simulated by a single “hinge” event. As depicted in Fig. 3, the product is first moved forward by a randomly chosen fraction of the distance s , where its direction of travel is then rotated by an angle randomly sampled from a probabilistic relation that describes multiple scattering. The electron is then transported the remaining fraction of s . To partially account for the energy dependence of elastic scattering, the energy loss and angular deflection are treated as independent processes and are simulated in random order. That is, the multiple scattering angle is sampled randomly at either the particle's energy at the beginning or ending of the step.

C. Photon simulation

After being produced by bremsstrahlung, photons are assumed subject to three interactions: Compton scattering, photoelectric absorption, and positron-electron pair

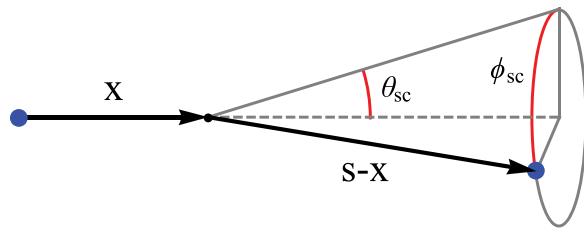


Fig. 3. Multiple scattering of an e^\pm using the random hinge method. The cumulative elastic scattering over path s is expressed as a scattering “hinge” that occurs at a single location within the path. Using a probabilistic relation derived in multiple-scattering theory, the polar scattering angle θ_{sc} is randomly sampled at either the particle's initial or final energy, and the particle's trajectory is rotated at the hinge point. The azimuthal multiple scattering angle ϕ_{sc} is assigned randomly from 0 to 2π , due to radial symmetry of the elastic scattering cross section.

production. Compton scattering is the dominant process at intermediate energies, while photoelectric absorption and pair production take over at low and high energies, respectively. Because photons may travel long distances before interacting, we simulate their interactions explicitly on an event-by-event basis.

For a photon with energy k , the interaction coefficient μ is calculated. Then, assuming the probability distribution of interaction after traveling a distance x is proportional to $e^{-\mu x}$, the distance s a given photon travels to the next interaction is randomly sampled from this distribution. If the traveling distance takes the photon outside of the detector, the photon is terminated, and the energy it carries is considered lost, i.e., not deposited in the detector. Otherwise, the interaction is simulated, the particle properties are modified accordingly, and the procedure repeats.

D. Simulation logic

Our program requires the following nine inputs to properly simulate the physics of energy deposition in the scintillator: radius of detector R_d , height of detector H_d , number of decay events N_{sim} , assumed muon rest mass $m_\mu c^2$, bremsstrahlung-photon production cutoff k_c , secondary-electron production cutoff T_c , maximum single-step fractional energy loss f , minimum allowed step size s_{min} , and electron/positron kinetic energy simulation cutoff T_{min} . Four other inputs configure operation of the simulation (e.g., precision level, energy partitioning size, and timeout setting).

The full simulation combines the product and photon transport procedures of Secs. IV A–IV C in order to generate simulated distributions of energy deposition. At the beginning of a simulation run, a list of N_{sim} product particles is generated, spatially distributed randomly and uniformly throughout the detector volume with random angular trajectories. The charges of these product particles are assigned randomly, in proportion to the known μ^+/μ^- ratio at sea level. The initial energies are assigned randomly and uniformly over the allowed range $0 \leq E_e \leq E_{max}$. Each product particle is then evolved by repeatedly stepping and tracking the product (and all produced secondary particles) until they either escape the detector or deposit all of their energy. One such tracking is depicted in Fig. 4 for an electron with an initial kinetic energy of 49.5 MeV.

Every tracked product particle has a *true* initial energy E_e and an *apparent* energy E_d (i.e., actual deposited energy). For example, in the event shown in Fig. 4, which is initiated by a product electron with $E_e = 49.5 \text{ MeV}$,²¹ the deposited energy $E_d = 37.9 \text{ MeV}$ and so the product's initial kinetic energy will appear in our experiment to be at this lower energy. To each tracked event, we assign a probability factor of $P(E_e)$ using Eq. (4). The probability factor recovers the underlying physics of muon decay by properly weighting the likelihood of events in accordance with Fermi theory. Thus, the program takes a list of N_{sim} product particles as input, and determines a set of N_{sim} weighted data points of the form $[E_d, P(E_e)]$. From this data set, a histogram is formed of the expected number $N_{sim}(E_d)$ of product particles with each of the allowed apparent energies. To aid comparison with experimental data, the horizontal axis of these simulation plots is given as the normalized apparent energy $\epsilon \equiv E_d/E_d^{max}$, i.e., E_d is normalized by its maximum value in the data set.

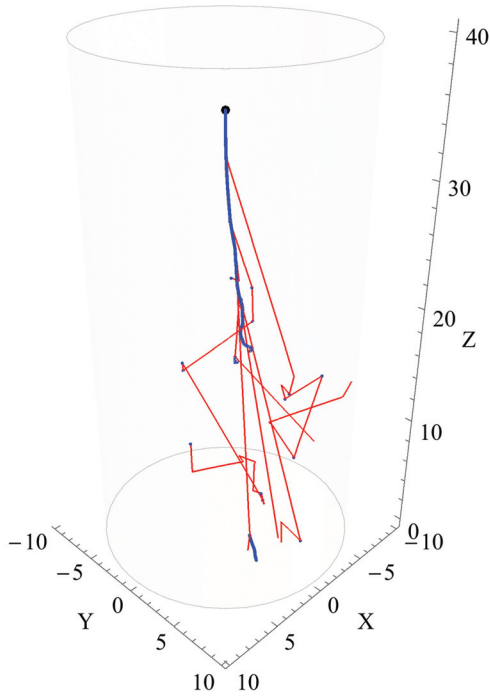


Fig. 4. Simulated particle tracks for an electron with initial kinetic energy of 49.5 MeV, spawned at $Z=35$ cm directed down along the detector's axis. Electron paths are darker (blue), while photons are lighter (red). Several processes are evident here including the production of secondary electrons, one of which escapes the detector with an energy of 3.8 MeV, and the escape of five unabsorbed photons carrying a total of 7.8 MeV out of the detector. The total deposited energy in the detector is 37.9 MeV.

V. RESULTS

In four extended runs, which took place over 516 total hours, about 2.4×10^6 muon-triggered oscilloscope traces were examined, resulting in a stored data set of 14,920 decay-event traces (i.e., in every trace, a product-pulse waveform was present). Each trace in this initial data set recorded our detector's response during the time window from 0.5 to $5.5 \mu\text{s}$ after the rising edge of the muon pulse and was evaluated as follows. Because the tailing portion of some muon pulses persisted slightly longer than our $0.5 \mu\text{s}$ trigger offset and since the temporal width of a complete product pulse was about $0.2 \mu\text{s}$, we eliminated traces from our data set in which the rising edge of the product pulse occurred within the first $0.2 \mu\text{s}$ or the last $0.2 \mu\text{s}$ of the trace. Applying these two criteria winnowed the number of traces in our data set down to $N_{\text{exp}} = 13,006$, where each trace represented our detector's response relative to a zero-level baseline during the time window from 0.7 to $5.3 \mu\text{s}$ after the muon trigger. Finally, for each of these remaining traces, we located the rising edge of the product pulse and then produced two numbers: the decay time t elapsed between the muon trigger and the product-pulse's rising edge, and the pulse area A found by numerically integrating the area under the product pulse over a $0.2 \mu\text{s}$ time interval.

A. Muon mass

For each product pulse, we take the quantity A as the measure of that product's apparent energy E_d in arbitrary units, i.e., $E_d \equiv A$. The histogram plot of the experimentally observed number $N_{\text{exp}}(E_d)$ of products with each allowed

apparent energy is given by the solid black curve in Fig. 5. Error bars on the data due to counting uncertainty are computed as the square root of the associated count number.

On this plot, the apparent energies are normalized according to $\epsilon \equiv E_d/E_d^{\text{max}}$ and divided into 10 equal-sized bins, where E_d^{max} is the maximum observed energy at the well-defined high-energy edge of the distribution of A -values. Ninety anomalous traces with randomly scattered energies greater than our chosen value of E_d^{max} were not included in the histogram plot. We attribute each of these high-energy outliers to two muons coincidentally passing through the detector within the time window of the trace acquisition (rather than due to a muon decay event) and justify neglecting these "false" traces for the reasons given in the Appendix. In addition, the missing data in the lowest bin below $\epsilon = 0.10$ are a result of the $3\times$ threshold for the waveform-maximum value we applied during data acquisition.

The Monte Carlo simulation was run for muon rest energies from $m_\mu c^2 = 80$ to 130 MeV in 5-MeV intervals, where $N_{\text{sim}} = 500,000$ for each run. The results of these runs can be compared with the experimental data in Fig. 5, where we have normalized the simulated distributions so that 13,006 ($= N_{\text{exp}}$) total events are included in the range $0.10 \leq \epsilon \leq 1.0$.

We use the following least-squares comparison method to determine which simulated distribution best matches our experimental data. For each distribution produced by the eleven values of $m_\mu c^2$, we first compare the experimentally determined $N_{\text{exp}}(\epsilon)$ with the predicted $N_{\text{sim}}(\epsilon)$ by calculating the residuals $r(\epsilon) = N_{\text{exp}}(\epsilon) - N_{\text{sim}}(\epsilon)$, and weight this value using the counting uncertainty. Then the weighted least-squares sum S is

$$S = \sum_{\epsilon} \left[\frac{N_{\text{exp}}(\epsilon) - N_{\text{sim}}(\epsilon)}{\sqrt{N_{\text{exp}}(\epsilon)}} \right]^2, \quad (5)$$

where the sum extends over the range $0.10 \leq \epsilon \leq 1.0$. In Fig. 6, we plot S vs $m_\mu c^2$, and obtain our "least-squares best-fit" value for the muon mass from the minimum of this plot. As shown, the minimum of S occurs for $m_\mu c^2 = 105$ MeV and is therefore our determined value for the muon mass, in close agreement to the accepted value of $m_\mu c^2 = 105.66$ MeV.

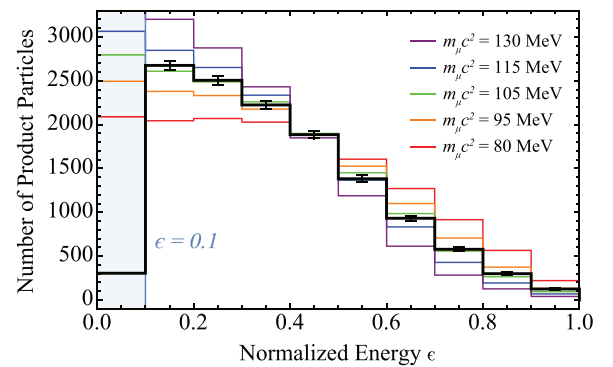


Fig. 5. Observed (black) and simulated (color-coded) distributions of normalized energy deposition plotted for comparison. Different colors represent a simulated distribution assuming the labeled muon rest mass $m_\mu c^2$. The low number of observed events in the region below $\epsilon = 0.1$ is an artifact of the $3\times$ threshold applied during data acquisition, so this region is ignored in our analysis.

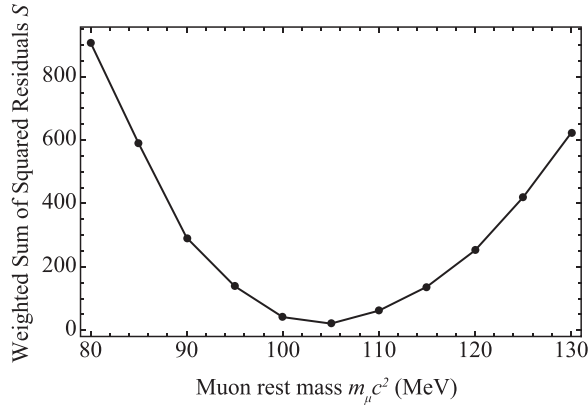


Fig. 6. The weighted sum of squared residuals S for each choice of $m_\mu c^2$ represents the degree to which the simulated distribution varies from the observed spectrum. A value of $m_\mu c^2 = 105$ MeV minimizes S , and is therefore our determined value for the muon mass.

B. Muon lifetime

To confirm that our data set was indeed produced by muon decay events, we made the histogram plot of the number of events observed with decay time t (sorted into 50 equal-sized bins) shown in Fig. 7. Consistent with Eq. (1), this plot is well fit by an exponential with lifetime $\tau_\mu = 2.09 \pm 0.04 \mu\text{s}$, a value in agreement with that found in other scintillation-based muon lifetime experiments. For such experiments, the measured lifetime is less than the free-space value $\tau_\mu = 2.197 \mu\text{s}$ due to the finite probability that the μ^- are captured by the scintillator's carbon atoms rather than undergoing spontaneous decay.^{1,6}

VI. CONCLUSION

As shown in Figs. 5 and 6, when our simulation is run under the assumption that $m_\mu c^2 = 105$ MeV, the values $N_{\text{exp}}(E_d)$ and $N_{\text{sim}}(E_d)$ are in very good agreement. To achieve this agreement, however, requires a detailed accounting of the many energy-loss mechanisms influencing the passage of product particles in a plastic scintillator. As one measure of the need for this level of precision, we find it not uncommon that $\sim 90\%$ of all photons produced by the slowing product particles escape the detector without being absorbed. Hence, a simple model such as that used in our spark-chamber experiment, which assumes all photons

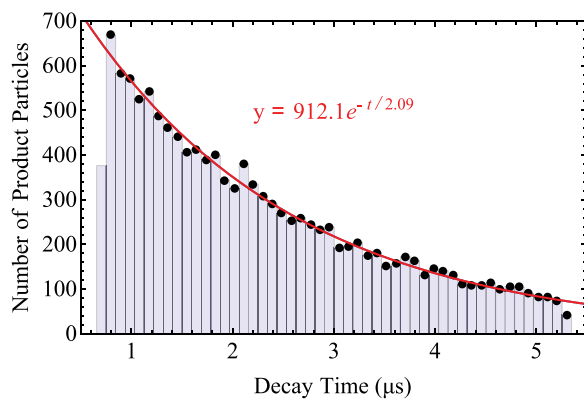


Fig. 7. Histogram plot of the number of events observed with decay time t . The decay times are sorted into 50 equal-sized bins. An exponential fit of this plot yields a lifetime value of $\tau_\mu = 2.09 \pm 0.04 \mu\text{s}$.

deposit their entire energy within the detector, will badly over-predict the value of E_d . In running our simulation, we noted that the minimum region in Fig. 6 is relatively flat over the region from 100 to 110 MeV and so we estimate our experimental value for $m_\mu c^2$ to be (105 ± 5) MeV, a range consistent with the accepted muon mass value.

ACKNOWLEDGMENTS

The authors would like to thank David Rogers and Ben Brau for helpful discussions. Also the authors are indebted to Chuck Hurlbut of Eljen Technology for his superb skill in designing, constructing, and testing our scintillation detector.

APPENDIX: FALSE TRACES DUE TO TWO-MUON COINCIDENCES

The muon flux rate at sea level exhibits a cosine-squared dependence on polar angle given by²²

$$I(\theta) = I_v \cos^2 \theta, \quad (\text{A1})$$

where $I_v = 0.007 \text{ cm}^{-2} \text{ s}^{-1} \text{ sr}^{-1}$. Using this relation, along with the dimensions of our cylindrically shaped detector, we find that the average rate at which muons enter our detector is $r = 30 \text{ s}^{-1}$. Following the discussion given in Ref. 1 (see p. 407, Eq. (9.31)), the rate R at which two muons will enter our detector within the observation window of $\Delta t = 5.3 \mu\text{s}$ is

$$R = \frac{r^2 \Delta t}{2} e^{-r \Delta t} \approx 8 \times 10^{-5} \text{ s}^{-1}. \quad (\text{A2})$$

Thus, over a run of $516 \text{ h} \approx 2 \times 10^6 \text{ s}$, we expect roughly 200 such events to produce traces within our data set. These “false” traces mimic, but are not due to, a muon decay event. In our analysis, each of these false traces will yield an apparent energy that is dependent on the energy deposited in the detector by the second muon. These apparent energies are expected to be distributed randomly in the range from nearly zero up to about 90 MeV (the energy loss associated with a muon traveling the longest possible distance through the detector). The 90 anomalous traces we eliminated from our data set are the subset of these false traces that, when analyzed, produced apparent energies E_d that were randomly and sparsely scattered at higher values than the sharp cutoff we empirically observe in the experimental distribution formed by the vast majority of our A -values.

^a)Electronic mail: jessick@reed.edu

¹Adrian C. Melissinos and Jim Napolitano, *Experiments in Modern Physics*, 2nd ed. (Academic Press, San Diego, 2003), pp. 399–409.

²R. E. Hall, D. A. Lind, and R. A. Ristinen, “A simplified muon lifetime experiment for the instructional laboratory,” *Am. J. Phys.* **38**, 1196–1200 (1970).

³A. Owens and A. E. Macgregor, “Simple technique for determining the mean lifetime of the cosmic ray μ meson,” *Am. J. Phys.* **46**, 859–860 (1978).

⁴Roger J. Lewis, “Automatic measurement of the mean lifetime of the muon,” *Am. J. Phys.* **50**, 894–895 (1982).

⁵T. Ward, M. Barker, J. Breeden, K. Komisarcik, M. Pickar, D. Wark, and J. Wiggins, “Laboratory study of the cosmic-ray lifetime,” *Am. J. Phys.* **53**, 542–546 (1985).

⁶Thomas Coan, Tiankuan Liu, and Jingbo Ye, “A compact apparatus for muon lifetime measurement and time dilation demonstration in the undergraduate laboratory,” *Am. J. Phys.* **74**, 161–164 (2006).

- ⁷ Experimental apparatus for muon lifetime experiment is available commercially from TeachSpin; a helpful user's manual can be downloaded at <http://www.matphys.com>.
- ⁸ Benjamin Brau, Christopher May, Robert Ormond, and John Essick, "Determining the muon mass in an instructional laboratory," *Am. J. Phys.* **78**, 64–70 (2010).
- ⁹ David J. Griffiths, *Introduction to Elementary Particles*, 2nd ed. (Wiley-VCH, Berlin, 2008), pp. 310–315.
- ¹⁰ E. Bartos, E. A. Kuraev, and M. Secansky, "Radiative corrections to muon decay in leading and next-to-leading approximation for electron spectrum," *Phys. Part. Nucl. Lett.* **6**, 365–367 (2009).
- ¹¹ Our scintillation detector was designed, constructed, and tested by Eljen Technology in Sweetwater, Texas USA.
- ¹² LabVIEW data-taking program is available from the authors upon request.
- ¹³ D. W. O. Rogers and A. F. Bielajew, "Monte Carlo techniques of electron and photon transport for radiation dosimetry," in *The Dosimetry of Ionizing Radiation*, Vol. III, edited by Kenneth R. Kase, Bengt E. Bjarnagard, and Frank H. Attix (Academic Press, San Diego, 1990), Chap. 5.
- ¹⁴ GEANT4 is "a toolkit for the simulation of the passage of particles through matter"; <https://geant4.web.cern.ch/geant4/>. The Physics Reference Manual is under the User Support/Documentation link.
- ¹⁵ EGSnrc is "a toolkit for Monte Carlo simulation of ionizing radiation transport"; <http://nrc-cnrc.github.io/EGSnrc/>. The user guide is at <http://nrc-cnrc.github.io/EGSnrc/doc/pirs701-egsnrc.pdf>.
- ¹⁶ PENELOPE performs Monte Carlo simulation of coupled electron-photon transport in arbitrary materials and complex quadric geometries"; <https://www.oecd-neo.org/abs/nea-1525.html>. See the user guide at <https://oecd-neo.org/science/docs/2011/nsc-doc2011-5.pdf>.
- ¹⁷ See supplementary material at <http://dx.doi.org/10.1119/1.4984811> for the MATHEMATICA code and a reference manual.
- ¹⁸ See the "Passage of particles through matter" section of *The Review of Particle Physics*; <http://pdg.lbl.gov>.
- ¹⁹ W. R. Leo, *Techniques for Nuclear and Particle Physics Experiments*, 2nd ed. (Springer-Verlag, Berlin, 1994), Chap. 2.
- ²⁰ Edwin A. Uehling, "Penetration of heavy charged particles in matter," *Ann. Rev. Nucl. Sci.* **4**, 315–350 (1954) (For heavy particles with unit charge, but e^\pm cross sections and stopping powers are also given).
- ²¹ This quoted value of E_e assumes a massless product electron. Our simulation actually accounts for the product's non-zero rest mass, which modifies the value of E_e slightly.
- ²² See the "Cosmic Rays" section of *The Review of Particle Physics*; <http://pdg.lbl.gov>.

ALL BACK ISSUES ARE AVAILABLE ONLINE

The contents of the *American Journal of Physics* are available online. AJP subscribers can search and view full text of AJP issues from the first issue published in 1933 to the present. Browsing abstracts and tables of contents of online issues and the searching of titles, abstracts, etc. is unrestricted. For access to the online version of AJP, please visit <http://aapt.org/ajp>.

Institutional and library ("nonmember") subscribers have access via IP addresses to the full text of articles that are online; to activate access, these subscribers should contact AIP, Circulation & Fulfillment Division, 800–344–6902; outside North American 516–576–2270 or subs@aip.org.

APPT (individual) members also have access to the American Journal of Physics Online. Not a member yet? Join today <http://www.aapt.org/membership/joining.cfm>. Sign up for your free Table of Contents Alerts at http://www.ajp.aapt.org/features/toc_email_alerts.